



Article

# Photosensing and Characterizing of the Pristine and In-, Sn-Doped Bi<sub>2</sub>Se<sub>3</sub> Nanoplatelets Fabricated by Thermal V–S Process

Chih-Chiang Wang <sup>1</sup>, Fuh-Sheng Shieu <sup>1,\*</sup> and Han C. Shih <sup>1,2,\*</sup>

<sup>1</sup> Department of Materials Science and Engineering, National Chung Hsing University, Taichung 40227, Taiwan; wilbur0913@gmail.com

<sup>2</sup> Department of Chemical Engineering and Materials Science, Chinese Culture University, Taipei 11114, Taiwan

\* Correspondence: fushshieu@dragon.nchu.edu (F.-S.S.); hcshih@mx.nthu.edu.tw (H.C.S.)

**Abstract:** Pristine, and In-, Sn-, and (In, Sn)-doped Bi<sub>2</sub>Se<sub>3</sub> nanoplatelets synthesized on Al<sub>2</sub>O<sub>3</sub>(100) substrate by a vapor–solid mechanism in thermal CVD process via at 600 °C under  $2 \times 10^{-2}$  Torr. XRD and HRTEM reveal that In or Sn dopants had no effect on the crystal structure of the synthesized rhombohedral-Bi<sub>2</sub>Se<sub>3</sub>. FPA–FTIR reveals that the optical bandgap of doped Bi<sub>2</sub>Se<sub>3</sub> was 26.3%, 34.1%, and 43.7% lower than pristine Bi<sub>2</sub>Se<sub>3</sub>. XRD, FESEM–EDS, Raman spectroscopy, and XPS confirm defects ( $In^{3+}_{Bi^{3+}}$ ), ( $In^{3+}_{V^0}$ ), ( $Sn^{4+}_{Bi^{3+}}$ ), ( $V^0_{Bi^{3+}}$ ), and ( $Sn^{2+}_{Bi^{3+}}$ ). Photocurrent that was generated in (In,Sn)-doped Bi<sub>2</sub>Se<sub>3</sub> under UV(8 W) and red (5 W) light revealed stable photocurrents of  $5.20 \times 10^{-10}$  and  $0.35 \times 10^{-10}$  A and high  $I_{photo}/I_{dark}$  ratios of 30.7 and 52.2. The rise and fall times of the photocurrent under UV light were  $4.1 \times 10^{-2}$  and  $6.6 \times 10^{-2}$  s. Under UV light, (In,Sn)-doped Bi<sub>2</sub>Se<sub>3</sub> had 15.3% longer photocurrent decay time and 22.6% shorter rise time than pristine Bi<sub>2</sub>Se<sub>3</sub>, indicating that (In,Sn)-doped Bi<sub>2</sub>Se<sub>3</sub> exhibited good surface conduction and greater photosensitivity. These results suggest that In, Sn, or both dopants enhance photodetection of pristine Bi<sub>2</sub>Se<sub>3</sub> under UV and red light. The findings also suggest that type of defect is a more important factor than optical bandgap in determining photo-detection sensitivity. (In,Sn)-doped Bi<sub>2</sub>Se<sub>3</sub> has greater potential than undoped Bi<sub>2</sub>Se<sub>3</sub> for use in UV and red-light photodetectors.

**Keywords:** Bi<sub>2</sub>Se<sub>3</sub>; nanoplatelets; defects; optical bandgap; photocurrent



**Citation:** Wang, C.-C.; Shieu, F.-S.; Shih, H.C. Photosensing and Characterizing of the Pristine and In-, Sn-Doped Bi<sub>2</sub>Se<sub>3</sub> Nanoplatelets Fabricated by Thermal V–S Process. *Nanomaterials* **2021**, *11*, 1352. <https://doi.org/10.3390/nano11051352>

Academic Editors:  
Maurizia Palumbo and  
Giacomo Giorgi

Received: 6 April 2021  
Accepted: 18 May 2021  
Published: 20 May 2021

**Publisher's Note:** MDPI stays neutral with regard to jurisdictional claims in published maps and institutional affiliations.



**Copyright:** © 2021 by the authors. Licensee MDPI, Basel, Switzerland. This article is an open access article distributed under the terms and conditions of the Creative Commons Attribution (CC BY) license (<https://creativecommons.org/licenses/by/4.0/>).

## 1. Introduction

Bi<sub>2</sub>Se<sub>3</sub> is a well-known second-generation topological insulator (TI) with a narrow bandgap of 0.35 eV and a rhombohedral crystal structure [1]. Se vacancies ( $v_{Se}$ ), which act as electron donors, are the main defects in the Bi<sub>2</sub>Se<sub>3</sub> structure, making it an n-type topological insulator [2]. The crystalline Bi<sub>2</sub>Se<sub>3</sub> is composed of layered structures; each layer consists of five stacked monoatomic layers, as in Se-Bi-Se'-Bi-Se, and is thus known as a quintuple layer (QL) [3]. Covalent bonds dominate the QL [4], whereas Van der Waals' forces dominate between QLs; hence, the dopants can be adequately intercalated among them [5]. A TI has an insulating bulk state and a topologically protected gapless surface state in three dimensions and an edge state in two dimensions, owing to spin-orbital coupling (SOC) and time-reversal symmetry (TRS) [6,7]. Both SOC and TRS suppress backscattering and reduce the sensitivity to surface impurities or defects when electrons are transported on the surface of a TI. These gapless states thus lead to a high electronic conductivity [8,9] and the following features: (1) photon-like electrons, (2) low power dissipation, (3) spin-polarized electrons, and (4) the quantum spin Hall effect [10–13]. Owing to TIs' unique electronic properties, they have many potential applications, including photodetectors [14], lasers [15], gas sensors [16], spintronic devices [17], magnetoelectronic devices [18], quantum computers [19], and topological superconductors [20]. Several methods are commonly used to synthesize TIs; they include chemical vapor deposition [21],

mechanical exfoliation [22], solvothermal synthesis [23], molecular beam epitaxy [24], atomic layer epitaxy [25], metal–organic chemical vapor deposition [26], pulsed laser deposition [27], magnetron sputtering [28], and the Bridgeman method [29].

Broadband photodetectors are made of potential materials, whose conductivity can be changed by incident light such as UV, visible, or IR light; they have photoabsorbance over a wide range of wavelengths, high photosensitivity, high carrier mobility, high conservation efficiency, operability at a low voltage, and long operational stability [30,31]. Photon–electron transfer is the primary detection mechanism of photodetectors [32]. Thus, photodetectors can be used as potential materials in optical information communication, imaging detection, and biodetectors [33,34]. As required for use in photodetectors, topological insulating  $\text{Bi}_2\text{Se}_3$  is a potential material and has fascinating optoelectronic properties, such as a tunable surface bandgap, a polarization-sensitive photocurrent, and thickness-dependent optical absorption [35]. Bulk  $\text{Bi}_2\text{Se}_3$  has a narrow bandgap of 0.35 eV and therefore a wide range of absorption wavelengths. However, its surface transportation can be suppressed by the free carriers that are presented in its bulk state. Shrinking to the nanoscale, as for nanoplates, nanowires, nanoribbons, and thin films, it suppresses the contribution of the bulk state to reduce the surface transportation, strengthening its surface transportation by increasing the surface-to-volume ratio [7,9]. Supplementary Table S1 lists  $\text{Bi}_2\text{Se}_3$ -based photodetectors.

The optical bandgap of  $\text{Bi}_2\text{Se}_3$  depends on the synthesizing conditions. Pejova et al. reported that chemically deposited  $\text{Bi}_2\text{Se}_3$  thin films have an optical bandgap energy of 2.3 eV [36]; Pramanik et al. fabricated  $\text{Bi}_2\text{Se}_3$  with optical bandgaps of 1.03 and 1.15 eV by chemical deposition [37]. Garcia et al. reported that chemically prepared  $\text{Bi}_2\text{Se}_3$  films had optical bandgaps of 1.41–1.7 eV and that postannealing (200 °C)  $\text{Bi}_2\text{Se}_3$  films had bandgaps of 1.06–1.57 eV [38]. Manjulavalli et al. found that  $\text{Bi}_2\text{Se}_3$  films that were prepared by thermal evaporation had an optical bandgap of 0.825 eV, and annealed films had a gap of 0.61 eV [39]. Augustine et al. reported that  $\text{Bi}_2\text{Se}_3$  films that were fabricated by thermal evaporation had an optical bandgap of 0.67 eV [40]. Alemi et al. synthesized  $\text{Bi}_2\text{Se}_3$  nanoplatelets, which had a bandgap of 2.95 eV, by a hydrothermal process [41]. These results reveal that the absorption range of  $\text{Bi}_2\text{Se}_3$  can be narrowed, affecting its photo-detective efficiency. According to the relevant literature, doping can modify the optical bandgaps of  $\text{Bi}_2\text{Se}_3$  nanostructures. Supplementary Table S2 presents the variations of bandgap energy of  $\text{Bi}_2\text{Se}_3$  that is doped with various dopants.

Bismuth (Bi, melting point = 271.4 °C), selenium (Se, melting point = 220 °C), indium (In, melting point = 156.6 °C), and tin (Sn, melting point = 231.9 °C) have similar melting points. The covalent radii of Bi (~148 pm), In (~142 pm), and Sn (~139 pm) are similar. The thermal–CVD process was used to synthesize pristine  $\text{Bi}_2\text{Se}_3$  nanoplatelets on  $\text{Al}_2\text{O}_3(100)$  substrates by the vapor–solid growth mechanism at 600 °C under  $1.2 \times 10^{-2}$  Torr. The photocurrents in In-, Sn-, and (In, Sn)-doped  $\text{Bi}_2\text{Se}_3$  nanoplatelets have not been studied. Dopants In and Sn are used herein to fabricate In-, Sn-, and (In, Sn)-doped  $\text{Bi}_2\text{Se}_3$  nanoplatelets. The types of defects and effects of In and Sn dopants on the  $\text{Bi}_2\text{Se}_3$  crystal structure were investigated by XRD, HRTEM, XPS, and Raman spectroscopy. The obtained optical bandgaps were estimated using an FPA–FTIR spectrometer. The photosensitivities were systematically obtained by measuring the photocurrents under UV and red light.

## 2. Materials and Methods

### 2.1. Synthesis of Pristine and In-, Sn-Doped $\text{Bi}_2\text{Se}_3$ Nanoplatelets

Supplementary Figure S1 schematically depicts the synthetic system. Pristine  $\text{Bi}_2\text{Se}_3$  nanoplatelets were synthesized on  $\text{Al}_2\text{O}_3(100)$  substrate ( $0.5 \times 0.5 \text{ mm}^2$ ) by the catalyst-free V–S mechanism using a thermally activated process in a quartz tube furnace. A 0.2 g mixture of precursor powders of high-purity 0.1 g Bi (Merck, 99%,  $4.78 \times 10^{-4}$  mole, Darmstadt, Germany) and 0.1 g Se (Alfa Aesar, 99%,  $1.27 \times 10^{-3}$  mole, Ward Hill, MA, USA) was placed on an alumina boat in the heating zone at the center of a quartz tube and heated at a rate of 25 °C/min under  $1.2 \times 10^{-2}$  Torr to 600 °C, which was maintained

for 60 min.  $\text{Al}_2\text{O}_3(100)$  substrate was placed upstream in the quartz tube at about  $150^\circ\text{C}$ , about 21 cm away from the alumina boat. The pristine  $\text{Bi}_2\text{Se}_3$  nanoplatelets thus formed were then deposited on the  $\text{Al}_2\text{O}_3(100)$  substrate. After the 60 min deposition process, the deposition system was subsequently cooled to room temperature. The starting materials of In-doped  $\text{Bi}_2\text{Se}_3$  were 0.1 g Bi, 0.1 g Se, and 25 mg of high-quality In as dopant (Alfa Aesar, 99.99%,  $2.17 \times 10^{-4}$  mole, USA); those of Sn-doped  $\text{Bi}_2\text{Se}_3$  included 25 mg Sn as dopant (Alfa Aesar, 99.8%,  $2.11 \times 10^{-4}$  mole, USA); that of (In, Sn)-doped  $\text{Bi}_2\text{Se}_3$  included 12.5 mg co-dopants In ( $1.09 \times 10^{-4}$  mole) and 12.5 mg Sn ( $1.05 \times 10^{-4}$  mole). The In-, Sn-, and (In, Sn)-doped  $\text{Bi}_2\text{Se}_3$  nanoplatelets were synthesized in the same manner as the pristine  $\text{Bi}_2\text{Se}_3$  nanoplatelets.

## 2.2. Characterization of Nanoplatelets

The phase and crystal structures of the undoped, as well as the In-, Sn-, and (In, Sn)-doped  $\text{Bi}_2\text{Se}_3$  nanoplatelets were determined using a mass absorption coefficient glancing incident X-ray diffractometer with an incidence angle of  $0.5^\circ$  ( $\lambda = 0.154$  nm, 30 A, 40 kV, Bruker D2 PHASER) and a high-resolution transmission electron microscope (JEOL, JEM-3000 F, Tokyo, Japan). The chemical binding energies and vibration modes of the chemical bonds were obtained using an X-ray photoelectron spectroscope (XPS, Perkin-Elmer model PHI1600 system, Waltham, MA, USA) and a Raman spectroscope (3D Nanometer Scale Raman PL Microspectrometer, Tokyo Instruments, Inc., Tokyo, Japan) with a semiconductor laser at an excitation wavelength of 633 nm. The surface morphology and EDS spectra were obtained using FESEM (ZEISS ULTRA PLUS, Carl Zeiss Microscopy GmbH, Oberkochen, Germany). The optical absorbance values were recorded using a focal plane array-FTIR spectrometer (FPA-FTIR, Bruker Vertex 70V, Hyperion 3000,  $64 \times 64$  MCT Focal Plane Array, Bruker Optik GmbH, Ettlingen, Germany).

## 2.3. Photocurrent Analysis

Photocurrents were measured using a semiconductor I-V property analyzer (Keysight B2901A Precision Source/Measure Unit 100 fA, Keysight Technologies, Santa Rosa, CA, USA) under irradiations of UV or the red light at atmospheric pressure and room temperature, while the bias voltage was kept at 0 V during the photocurrent measuring. The irradiation sources were 30 cm long UV (8 W,  $\lambda = 365$  nm) and red (5 W,  $\lambda = 700$ – $900$  nm) LED lamps. The distance between each lamp and the sample was 20 cm. Supplementary Figure S2 schematically depicts the photocurrent measuring system. The sample was placed in a closed box/darkroom to eliminate any effect of ambient light. The silver paste was dropped and deposited onto the surface of each sample of the nanoplatelets and connected to the photocurrent analyzer using copper wires. The photocurrent of each sample was measured in five runs; in each run, the light was on for 10 s and off for 10 s.

## 3. Results

### 3.1. XRD Analysis

Figure 1a presents the XRD patterns of the pristine and In-, Sn-, and (In, Sn)-doped  $\text{Bi}_2\text{Se}_3$  nanoplatelets. These nanoplatelets have the typical rhombohedral  $\text{Bi}_2\text{Se}_3$  structure (JCPDS 89-2008). Table 1 presents the lattice constants  $a$ ,  $b$ ,  $c$ , and the  $c/a$  ratio. The lattice constants are calculated as the formula  $\frac{1}{d_{(hkl)}^2} = \left[ \frac{4}{3}(h^2 + k^2 + hk) + l^2 \left(\frac{a}{c}\right)^2 \right] \frac{1}{a^2}$ , where  $h$ ,  $k$ , and  $l$  are the Miller indices, and  $a$  and  $c$  are the lattice constants. For the In-, Sn-, and (In, Sn)-doped  $\text{Bi}_2\text{Se}_3$  nanoplatelets, lattice constant  $a$  deviates by  $-1.312$ ,  $-0.037$ , and  $-1.776\%$ , respectively, and lattice constant  $c$  deviates by  $0.315$ ,  $-2.339$ , and  $0.148\%$ , respectively, from their values for the undoped nanoplatelets. The decreases in  $a$  are attributed to the substitution of Bi (covalent radius:  $148 \pm 4$  pm) rather than Se (covalent radius:  $120 \pm 4$  pm) by the In (covalent radius:  $142 \pm 5$  pm) or Sn (covalent radius:  $139 \pm 4$  pm) dopant. The lowering of  $c$  by doping with Sn is attributed to the substitution of Bi by Sn [42]. The bond length of Bi-Se is  $2.86/3.05$  Å, and the gap between each QL is  $2.62$  Å [43]; therefore, the increase in  $c$  upon doping with In or (In, Sn) is attributable to

the intercalation of In atoms between the QLs [44]. The decrease and increase of the lattice constants  $a$  and  $c$ , respectively, imply that the In and Sn dopants affected the crystallinity of the  $\text{Bi}_2\text{Se}_3$  nanoplatelets. Defects are formed by In at Bi lattice sites ( $\text{In}_{\text{Bi}}$ ), Sn at Bi lattice sites ( $\text{Sn}_{\text{Bi}}$ ), and In in vacancies ( $\text{In}_V$ ).

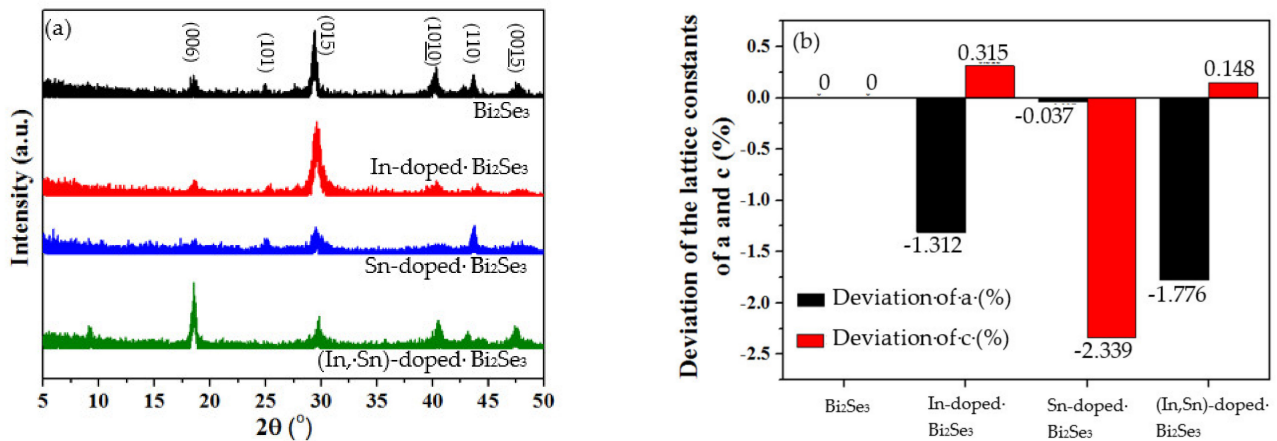


**Figure 1.** (a) XRD patterns and (b) deviations of the lattice constants  $a$  and  $c$  of pristine, and In-, Sn-, and (In, Sn)-doped  $\text{Bi}_2\text{Se}_3$  nanoplatelets.

**Table 1.** Lattice constants  $a$  and  $c$ ,  $c/a$  ratios of pristine, and In-, Sn-, and (In, Sn)-doped  $\text{Bi}_2\text{Se}_3$  nanoplatelets.

Sample	Lattice Constant		$c/a$ Ratio	Concentration ( $\times 10^{-4}$ Mole)			
	$a (=b)$	$c$		Bi	Se	In	Sn
$\text{Bi}_2\text{Se}_3$	0.4142	2.8677	6.9236	4.78	12.7	0	0
In-doped $\text{Bi}_2\text{Se}_3$	0.4088	2.8767	7.0378	4.78	12.7	2.17	0
Sn-doped $\text{Bi}_2\text{Se}_3$	0.4140	2.8006	6.7641	4.78	12.7	0	2.11
(In, Sn)-doped $\text{Bi}_2\text{Se}_3$	0.4068	2.8719	7.0593	4.78	12.7	1.09	1.05

### 3.2. Structural and Surface Morphology Analyses

Figure 2a–d and the respective thickness of Figure S3a–d show the cross-sectional and the plane-view images of pristine and In-, Sn-, and (In,Sn)-doped  $\text{Bi}_2\text{Se}_3$  nanoplatelets, respectively. The overall thickness of the samples of pristine and In-, Sn-, and (In, Sn)-doped  $\text{Bi}_2\text{Se}_3$  nanoplatelets are, respectively, of the 3.391, 0.859, 1.066, and 0.563  $\mu\text{m}$ , as shown in Figure S3a–d. The hexagonal  $\text{Bi}_2\text{Se}_3$  nanoplatelets (Figure 2a and Figure S3a) appear in similar morphologies after the doping.

The In- (Figure 2b and Figure S3b) and (In,Sn)-doped  $\text{Bi}_2\text{Se}_3$  (Figure 2d and Figure S3d) reveal less well-defined hexagonal structures; however, the Sn-doped  $\text{Bi}_2\text{Se}_3$  (Figure 2c and Figure S3c) exhibits a very well-defined hexagonal structure. On average, the  $\text{Bi}_2\text{Se}_3$  nanoplatelets are unequivocally hexagonal-like in shape, typical of the rhombohedral structure. The average thickness (40 nanoplatelets) and average diameter (40 nanoplatelets) of the pristine and In-, Sn-, and (In, Sn)-doped  $\text{Bi}_2\text{Se}_3$  nanoplatelets are, respectively, listed in Table 2.

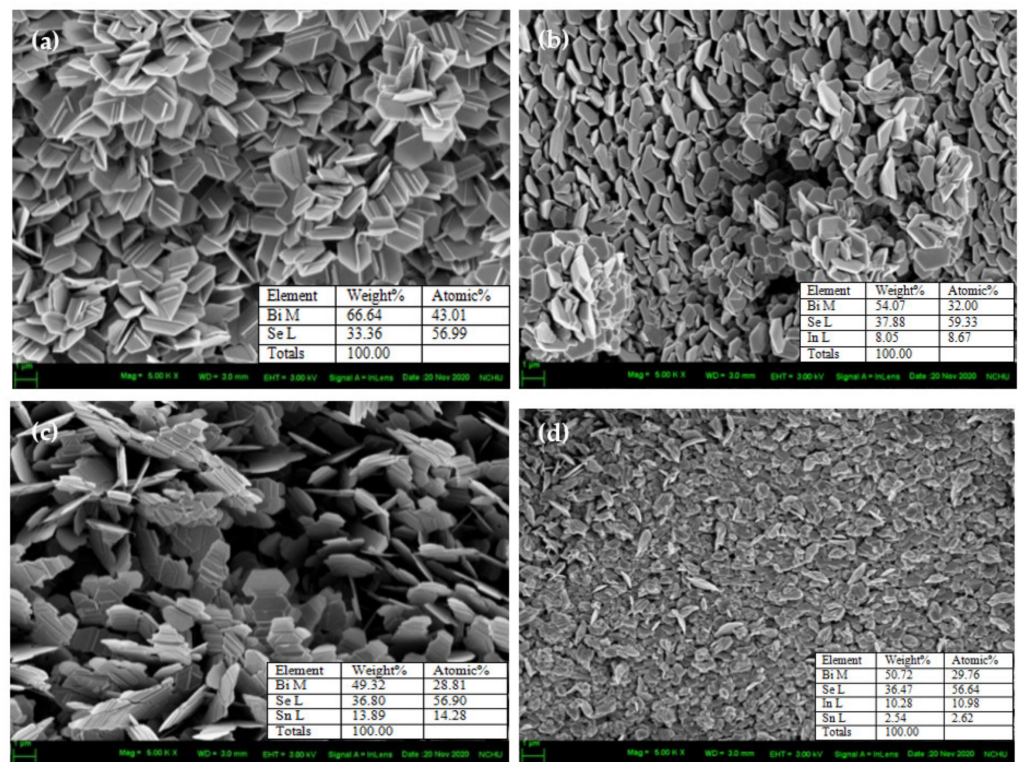


**Figure 2.** FESEM images and EDS results of (a) pristine, (b) In-, (c) Sn-, and (d) (In, Sn)-doped  $\text{Bi}_2\text{Se}_3$  nanoplatelets.

**Table 2.** Average diameter, average thickness, and FESEM–EDS of Bi, Se, In, and Sn (atomic percent, at.%) of pristine, and In-, Sn-, and (In, Sn)-doped  $\text{Bi}_2\text{Se}_3$  nanoplatelets.

Sample	Average Diameter ( $\mu\text{m}$ )	Average Thickness (nm)	Bi (at.%)	Se (at.%)	In (at.%)	Sn (at.%)	Bi: Se
$\text{Bi}_2\text{Se}_3$	1.319	17.5	43.01	56.99	0.00	0.00	1:1.325
In-doped $\text{Bi}_2\text{Se}_3$	0.965	21.8	32.00	59.33	8.05	0.00	1:1.854
Sn-doped $\text{Bi}_2\text{Se}_3$	0.912	39.8	28.81	56.90	0.00	14.28	1:1.975
(In, Sn)-doped $\text{Bi}_2\text{Se}_3$	0.317	31.5	29.76	56.64	10.98	2.62	1:1.903

Table 2 shows EDS results for Bi, Se, In, and Sn, which reveal that the ratio Bi:Se increases upon the addition of dopants. This result is attributable to the substitution of Bi by In and/or Sn dopants. Under the Se-rich condition (mole ratio,  $\text{Bi}/\text{Se} = 0.755$ ) in this work, the formation energy of  $V_{\text{Se}}$  defects increases from 1.14 to 2.16 eV, and that of  $V_{\text{Bi}}$  decreases from 4.13 to 2.60 eV [42]; Bi is thus determined to be substituted by In and/or Sn dopants, consistent with the XRD results. Figure 3 presents the HRTEM images and SAD patterns of pristine (Figure 3a), and In- (Figure 3b), Sn- (Figure 3c), and (In, Sn)-doped  $\text{Bi}_2\text{Se}_3$  nanoplatelets (Figure 3d). Table 3 provides d-spacings and diffraction planes. These results are consistent with the rhombohedral  $\text{Bi}_2\text{Se}_3$  structure and confirm that the dopants, such as In and Sn, have no effect on the crystal structure of  $\text{Bi}_2\text{Se}_3$ .

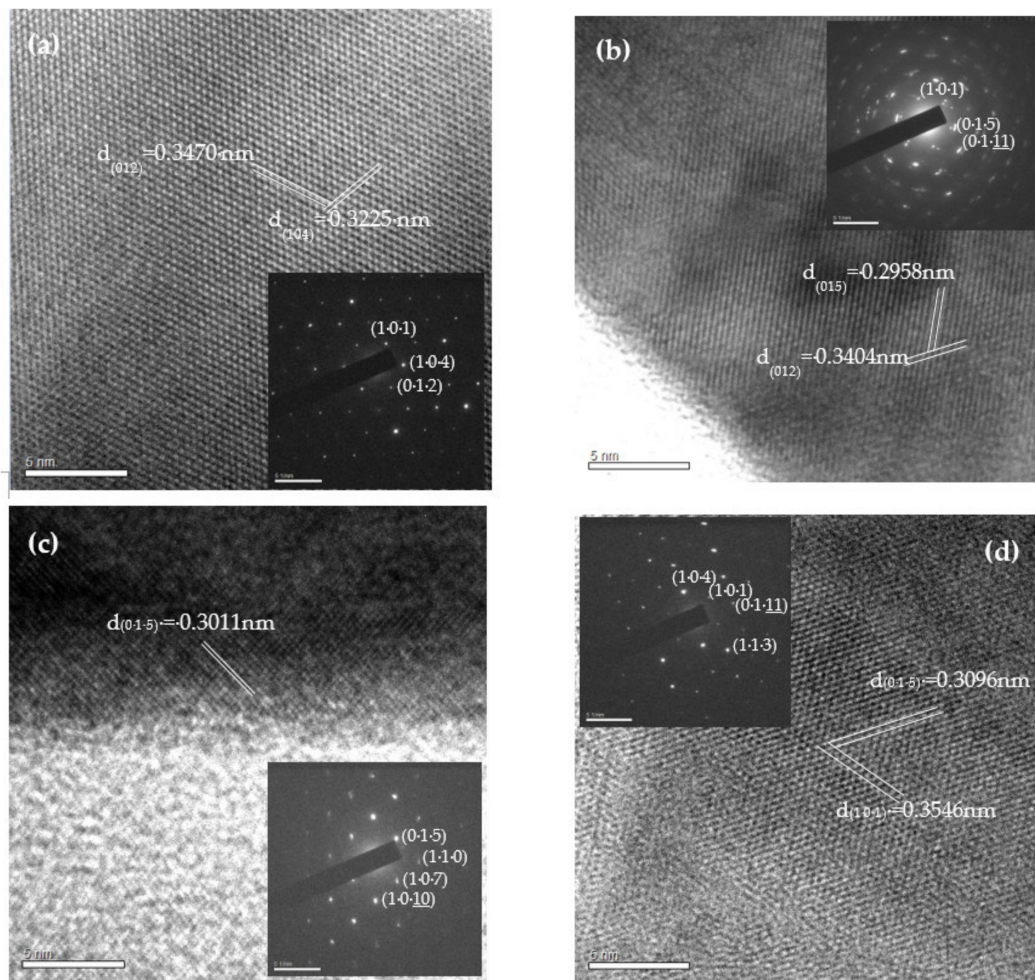


**Figure 3.** HRTEM images and SAD patterns of (a) Bi<sub>2</sub>Se<sub>3</sub>, (b) In-, (c) Sn-, and (d) (In, Sn)-doped Bi<sub>2</sub>Se<sub>3</sub> nanoplatelets.

**Table 3.** The d-spacings and diffracted planes of pristine, and In-, Sn-, and (In, Sn)-doped Bi<sub>2</sub>Se<sub>3</sub> nanoplatelets.

Sample	High-Resolution Images		SAD Patterns
	d-Spacings (nm)	Planes	Diffracted Planes
Bi <sub>2</sub> Se <sub>3</sub>	0.3470	(0 1 2)	(1 0 1)
	0.3225	(1 0 4)	(0 1 2)
In-doped Bi <sub>2</sub> Se <sub>3</sub>	0.3404	(0 1 2)	(1 0 4)
	0.2958	(0 1 5)	(1 0 1)
Sn-doped Bi <sub>2</sub> Se <sub>3</sub>	0.3011	(0 1 5)	(0 1 11)
			(0 1 5)
			(1 0 7)
			(1 0 10)
(In, Sn)-doped Bi <sub>2</sub> Se <sub>3</sub>	0.3546	(1 0 1)	(1 1 0)
	0.3096	(0 1 5)	(1 0 1)
			(1 0 4)
			(0 1 11)
			(1 1 3)

### 3.3. XPS Analysis

Figure 4 presents the XPS results for Bi 4f, Se 3d, In 3d, and Sn 3d. Figure 4a shows the binding energy of Bi 4f. Peaks at 157.9 and 163.2 eV are attributed to the Bi 4f<sup>7/2</sup> and Bi 4f<sup>5/2</sup> orbitals in the Bi<sub>2</sub>Se<sub>3</sub> phase [45]. Binding energies 159.1 and 164.3 eV are associated with the Bi 4f<sup>7/2</sup> and Bi 4f<sup>5/2</sup> orbitals in the Bi<sub>2</sub>O<sub>3</sub> phase [46,47]. Figure 4b presents the XPS spectra of Se 3d<sup>5/2</sup> and Se 3d<sup>3/2</sup> and the binding energies of 53.6 and 54.6 eV are associated with the Bi<sub>2</sub>Se<sub>3</sub> phase [45]. The peak at 58.9 eV is attributed to the SeO<sub>2</sub> phase [48,49]. The samples are stored in the ambient environment, causing the Bi<sub>2</sub>O<sub>3</sub> and SeO<sub>2</sub> phases to form on the surface of the nanoplatelets. These results confirm the formation of the Bi<sub>2</sub>Se<sub>3</sub> phase by the thermal V–S mechanism. Figure 4c displays the binding energies of the In 3d<sup>5/2</sup> and In 3d<sup>3/2</sup> orbitals, 444.7 and 452.3 eV, associated with the In–Se bond [50]. This finding reveals that In<sup>3+</sup> was doped into the Bi<sub>2</sub>Se<sub>3</sub> structure. The typical Bi<sub>2</sub>Se<sub>3</sub> structure consists of a stack of several quintuple layers (QLs). Each QL comprises Se–Bi–Se–Bi–Se. In<sup>3+</sup> has two possible positions as a dopant: (1) In<sup>3+</sup> may substitute at the Bi<sup>3+</sup> lattice sites, producing the neutral defect ( $In^{3+}_{Bi^{3+}}$ ) and (2) In<sup>3+</sup> intercalates between pairs of QLs, indicating the possible formation of potentially forming the donor defect ( $In^{3+}_V$ ), where V is the vacancy in the Van der Waals gap. Therefore, In–Se bonds form inside the Bi<sub>2</sub>Se<sub>3</sub> structure or between QLs. The peak at 441.5 eV is ascribed to the Bi<sup>3+</sup> 4d<sup>5/2</sup> orbital [51]. Figure 4d presents XPS spectra of Sn 3d. Peaks at 485.1 and 493.7 eV are associated with the Sn<sup>2+</sup> 3d<sup>5/2</sup> and Sn<sup>2+</sup> 3d<sup>3/2</sup> orbitals, respectively, of the SnSe phase [52]. Peaks at 486.6 and 495.1 eV are associated with the Sn<sup>4+</sup> 3d<sup>5/2</sup> and Sn<sup>4+</sup> 3d<sup>3/2</sup> orbitals of the SnSe<sub>2</sub> phase [53]. Accordingly, the Sn dopants substitute at some of the Bi lattice sites within the Bi<sub>2</sub>Se<sub>3</sub> crystal structure and bond with Se to form Sn–Se bonds. The integral area of the Sn<sup>4+</sup> in the XPS spectrum exceeds that of Sn<sup>2+</sup> (as shown in Figure 4d), implying that the Sn<sup>4+</sup> contents are higher than the Sn<sup>2+</sup> content. The XRD results reveal that the defect ( $Sn_{Bi}$ ) is formed in the Bi<sub>2</sub>Se<sub>3</sub> structure during the thermal V–S process. The concentration of the donor defects ( $Sn^{4+}_{Bi^{3+}}$ ) should be higher than those of the acceptor defects ( $Sn^{2+}_{Bi^{3+}}$ ).

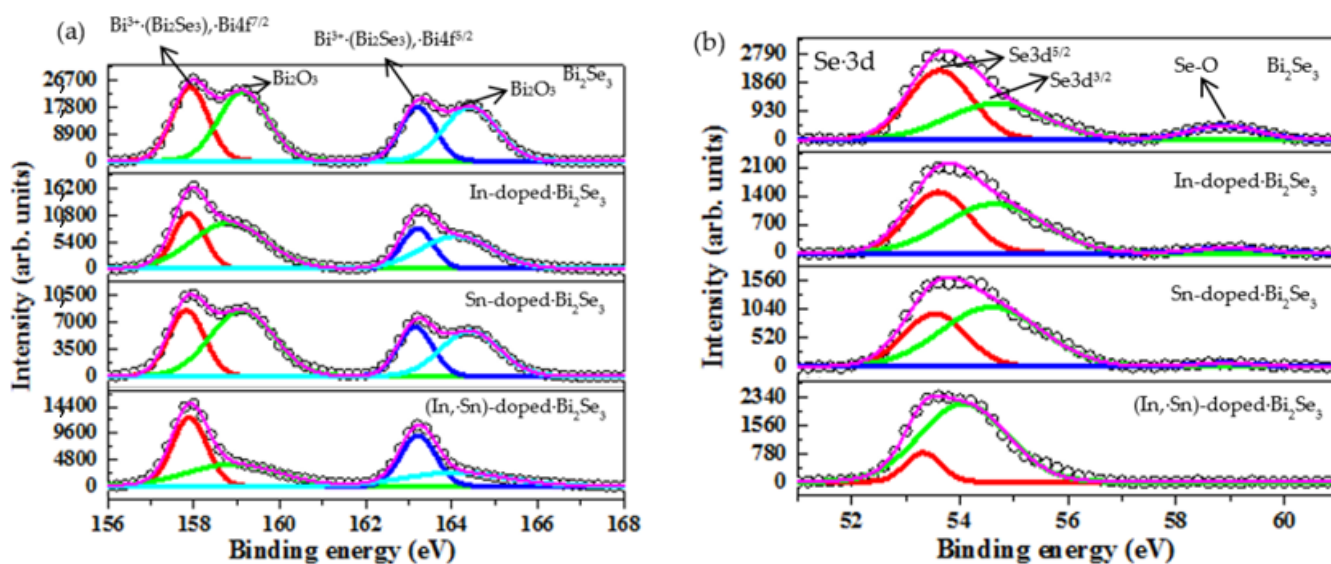


Figure 4. Cont.

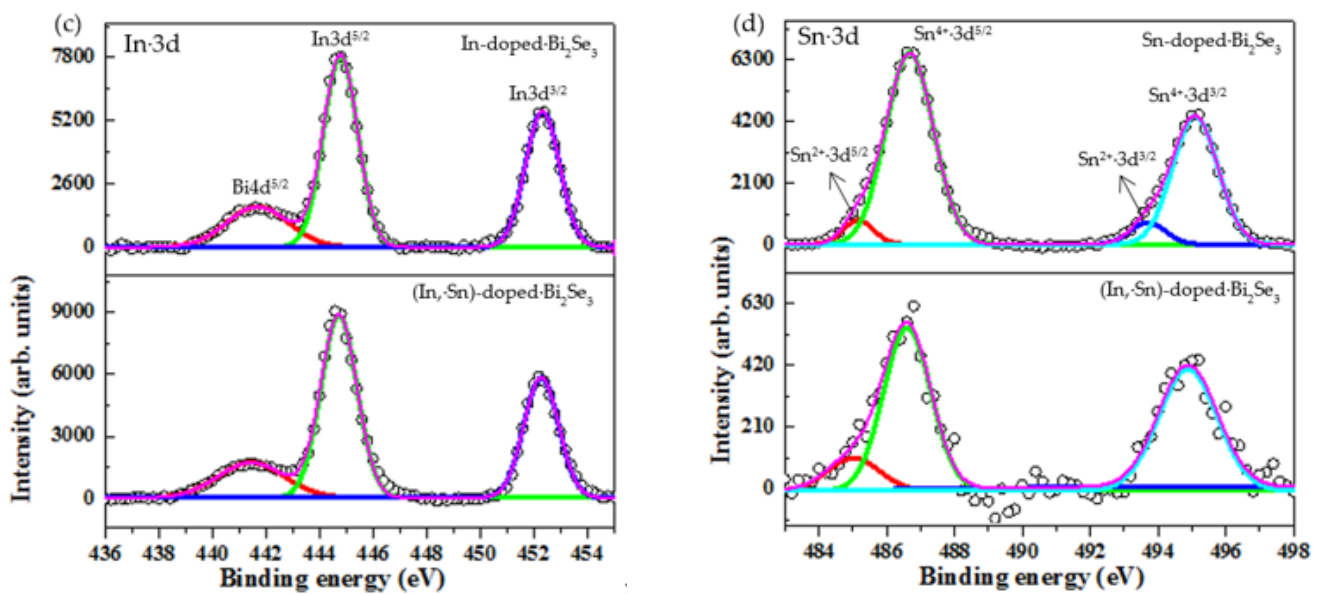


Figure 4. XPS spectra of (a) Bi 4f, (b) Se 3d, (c) In 3d, and (d) Sn 3d in pristine, and Sn-, and (In, Sn)-doped  $\text{Bi}_2\text{Se}_3$  nanoplatelets.

### 3.4. Raman Spectra

Figure 5a presents the typical Raman active mode at  $A_{1g}^1$ ,  $E_g^2$ , and  $A_{1g}^2$  of the rhombohedral  $\text{Bi}_2\text{Se}_3$  structure [6,54]. No other peaks besides Bi-Se vibrational modes are observed; hence, the dopant does not change the crystal structure of the nanoplatelets or form a second-phase compound, consistent with the XRD results. The formation of  $\text{Bi}_2\text{Se}_3$  nanoplatelets is thus confirmed.

The typical structure of  $\text{Bi}_2\text{Se}_3$  is layered; each layer comprises five monoatomic planes and is, therefore, a quintuple layer (QL). The QL is denoted as A1-B1-A1'-B1-A1, as shown in Figure 5b [55]. A1 and A1' are the Se atoms; B1 is the Bi atom. Covalent bonds dominate the binding within each QL; Van der Waals' forces dominate the bonds between QLs [4,5]. The inset in Figure 5a schematically depicts the Raman peaks of  $A_{1g}^1$ ,  $E_g^2$ , and  $A_{1g}^2$  [56].  $A_{1g}^1$  is a symmetric out-of-plane stretching mode associated with the vibration of A1-B1 atoms in the same ( $A_{1g}^1$  mode) or the opposite ( $A_{1g}^2$  mode) direction.  $A_{1g}^2$  has a shorter atomic displacement than  $A_{1g}^1$ . Therefore, the  $A_{1g}^2$  mode has higher phonon energy than the  $A_{1g}^1$  mode [56].  $E_g^2$  is a symmetric in-plane bending mode and shearing the upper two layers of A1-B1 atoms that vibrate in the opposite direction increasing the atomic displacement to a value greater than that in the  $A_{1g}^2$  mode but smaller than that in the  $A_{1g}^1$  mode. Thus, the  $E_g^2$  mode has a phonon energy between those of the  $A_{1g}^2$  and  $A_{1g}^1$  modes [56].

Figure 5c shows the variations in characteristic Raman peaks at  $A_{1g}^1$ ,  $E_g^2$ , and  $A_{1g}^2$  with the species of dopant. A comparison with pristine  $\text{Bi}_2\text{Se}_3$  nanoplatelets reveals that both In and Sn dopants cause a redshift of the peaks of  $A_{1g}^1$ ,  $E_g^2$ , and  $A_{1g}^2$ , whereas (In, Sn) co-dopants do not shift the  $A_{1g}^2$  or  $E_g^2$  peak but do cause a redshift in the  $A_{1g}^1$  peak. Table 4 presents the Raman peaks of pristine and doped  $\text{Bi}_2\text{Se}_3$  nanoplatelets, showing the redshifts with the various dopants. The redshifts of the Raman peaks are frequently suggested to involve the heavier atomic weight and/or high-electronegativity dopant to be doped in [57]. The atomic weights of Bi, Se, In, and Sn are 209.0, 78.76, 114.8, and 118.7 (g/mole), and their electronegativities are 2.02, 2.55, 1.96, and 1.78, respectively. The Raman peaks of the doped  $\text{Bi}_2\text{Se}_3$  nanoplatelets thus exhibit a redshift. As shown in Table 4,  $E_g^2$ ,  $A_{1g}^2$ , and especially  $A_{1g}^1$  peaks are significantly redshifted by the addition of different dopants. The redshift is attributed to the substitution of Bi with dopant In or Sn, which has less weight and a lower electronegativity.

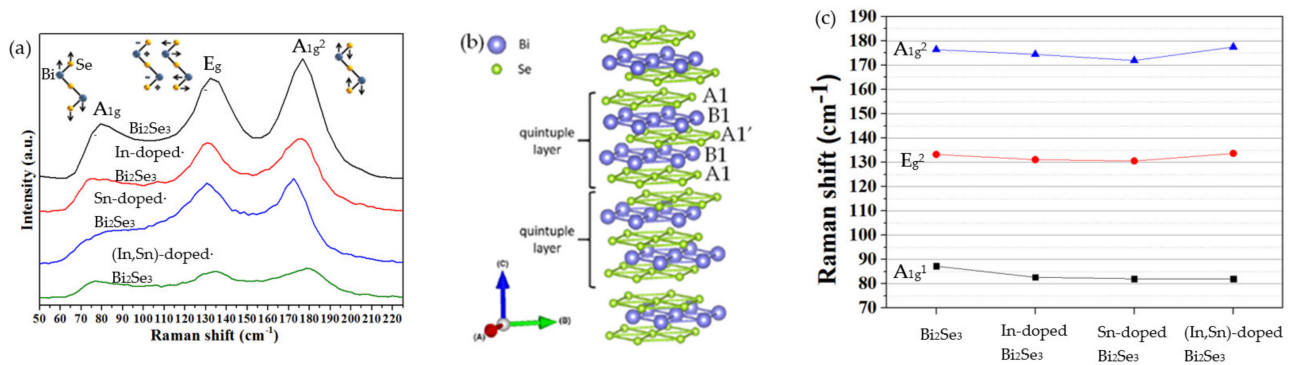


**Figure 5.** (a) Raman spectra of pristine, and In-, Sn-, and (In, Sn)-doped  $\text{Bi}_2\text{Se}_3$  nanoplatelets; the inset is the schematic vibration modes of  $A_{1g}^1$ ,  $E_g^2$ , and  $A_{1g}^2$  [56,58]. (b) Schematic layered structure of  $\text{Bi}_2\text{Se}_3$  [55]. (c) Variations of Raman shift at  $A_{1g}^1$ ,  $E_g^2$ , and  $A_{1g}^2$  with different dopants.

**Table 4.** Characteristic Raman peaks of the pristine, and In-, Sn-, and (In, Sn)-doped  $\text{Bi}_2\text{Se}_3$  nanoplatelets.

Sample	Raman Shift ( $\text{cm}^{-1}$ )		
	$A_{1g}^1$	$E_g^2$	$A_{1g}^2$
$\text{Bi}_2\text{Se}_3$	87.21	133.21	176.36
In-doped $\text{Bi}_2\text{Se}_3$	82.65	131.10	174.43
Sn-doped $\text{Bi}_2\text{Se}_3$	82.02	130.54	171.90
(In, Sn)-doped $\text{Bi}_2\text{Se}_3$	81.93	133.64	177.48

### 3.5. Photocurrent under UV and Red Light

#### 3.5.1. Analysis under UV and Red Illumination

Figure 6a shows the photocurrents in undoped, as well as In-, Sn-, and (In, Sn)-doped  $\text{Bi}_2\text{Se}_3$  nanoplatelets under UV light. All samples pass a photocurrent ( $I_{\text{photo}}$ ) that increases rapidly from  $I_{\text{dark}}$  ( $\sim 0.62 \times 10^{-11}$ – $1.65 \times 10^{-11}$  A) to the maximum  $I_{\text{max}}$  ( $\sim 8 \times 10^{-10}$ – $1 \times 10^{-9}$  A) and then suddenly falls to a stable value ( $I_{\text{stable}}$ ) when the light is turned on.  $I_{\text{stable}}$  is clearly independent of the exposure time and, for the undoped, and In-, Sn-, and (In, Sn)-doped  $\text{Bi}_2\text{Se}_3$  nanoplatelets, it is  $0.40 \times 10^{-10}$ ,  $0.65 \times 10^{-10}$ ,  $1.60 \times 10^{-10}$ , and  $5.20 \times 10^{-10}$  A, respectively, indicating that the dopants can increase the photocurrent of the pristine  $\text{Bi}_2\text{Se}_3$  nanoplatelets. In particular, the co-dopants In and Sn increase it by a factor of more than 13 to, for example,  $5.20 \times 10^{-10}$  A. The  $I_{\text{photo}}/I_{\text{dark}}$  ratios in the undoped, and In-, Sn-, and (In, Sn)-doped  $\text{Bi}_2\text{Se}_3$  nanoplatelets are, respectively, estimated as 7.66, 9.29, 15.8, and 30.7, as shown in Figure S4a and listed in Table 5, implying that the co-dopants of In and Sn enhance the photoresponsibility of the  $\text{Bi}_2\text{Se}_3$  nanoplatelets 4.01 times, which is higher than the pristine one. The decay of the current  $\Delta I_{\text{decay}}$  ( $I_{\text{max}} - I_{\text{stable}}$ ) in the undoped, as well as In-, Sn-, and (In, Sn)-doped  $\text{Bi}_2\text{Se}_3$  nanoplatelets, is  $8.33 \times 10^{-10}$ ,  $9.33 \times 10^{-10}$ ,  $7.76 \times 10^{-10}$ , and  $3.21 \times 10^{-10}$  A, respectively. A smaller  $\Delta I_{\text{decay}}$  is attributed to a longer electron lifetime and a higher concentration of electrons. Both the rise time ( $\tau_r$ ) and fall time ( $\tau_f$ ) are taken by the photocurrent to rise or to fall from 10% to 90% or from 90% to 10%, respectively, of its maximum photocurrent value, as an example of the (In,Sn)-doped  $\text{Bi}_2\text{Se}_3$  in Figure 6c. The average  $\tau_r$  for the undoped, and In-, Sn-, and (In, Sn)-doped  $\text{Bi}_2\text{Se}_3$  nanoplatelets are, respectively, evaluated as 0.053, 0.051, 0.044, and 0.041 sec; the average  $\tau_f$  are 0.049, 0.050, 0.054, and 0.066 sec. A shorter  $\tau_r$  is attributable to the higher photosensitivity. The decay time ( $t_{\text{decay}}$ ) is taken from the  $I_{\text{max}}$  to  $I_{\text{stable}}$ , which depends on the recombination rate of the photo-induced electrons and holes [59]. The average  $t_{\text{decay}}$  of the undoped, and In-, Sn-, and (In, Sn)-doped  $\text{Bi}_2\text{Se}_3$  nanoplatelets are estimated as 0.091, 0.097, 0.099, and 0.105 sec. A longer  $t_{\text{decay}}$  corresponds to slower recombination. Therefore, the co-dopants of In and Sn suppress the recombination rate of the photoinduced electrons and holes in the pristine  $\text{Bi}_2\text{Se}_3$  nanoplatelets. The detailed variations of the  $\log_{10}(\text{time})$

versus the photocurrents, which are recorded in the first run of the light-on/light-off cycle, between the pristine, and In-, Sn-, and (In,Sn)-doped  $\text{Bi}_2\text{Se}_3$  nanoplatelets are presented in Figure 6c. Table 5 presents relevant details. These results suggest that the dopants, and especially the co-dopants In and Sn, in  $\text{Bi}_2\text{Se}_3$  nanoplatelets, have various favorable effects, which are (1) extending the electron lifetime, (2) increasing the electron concentration, (3) promoting surface electronic transportation, and (4) improving the photo-sensitivity of the  $\text{Bi}_2\text{Se}_3$  nanoplatelets.

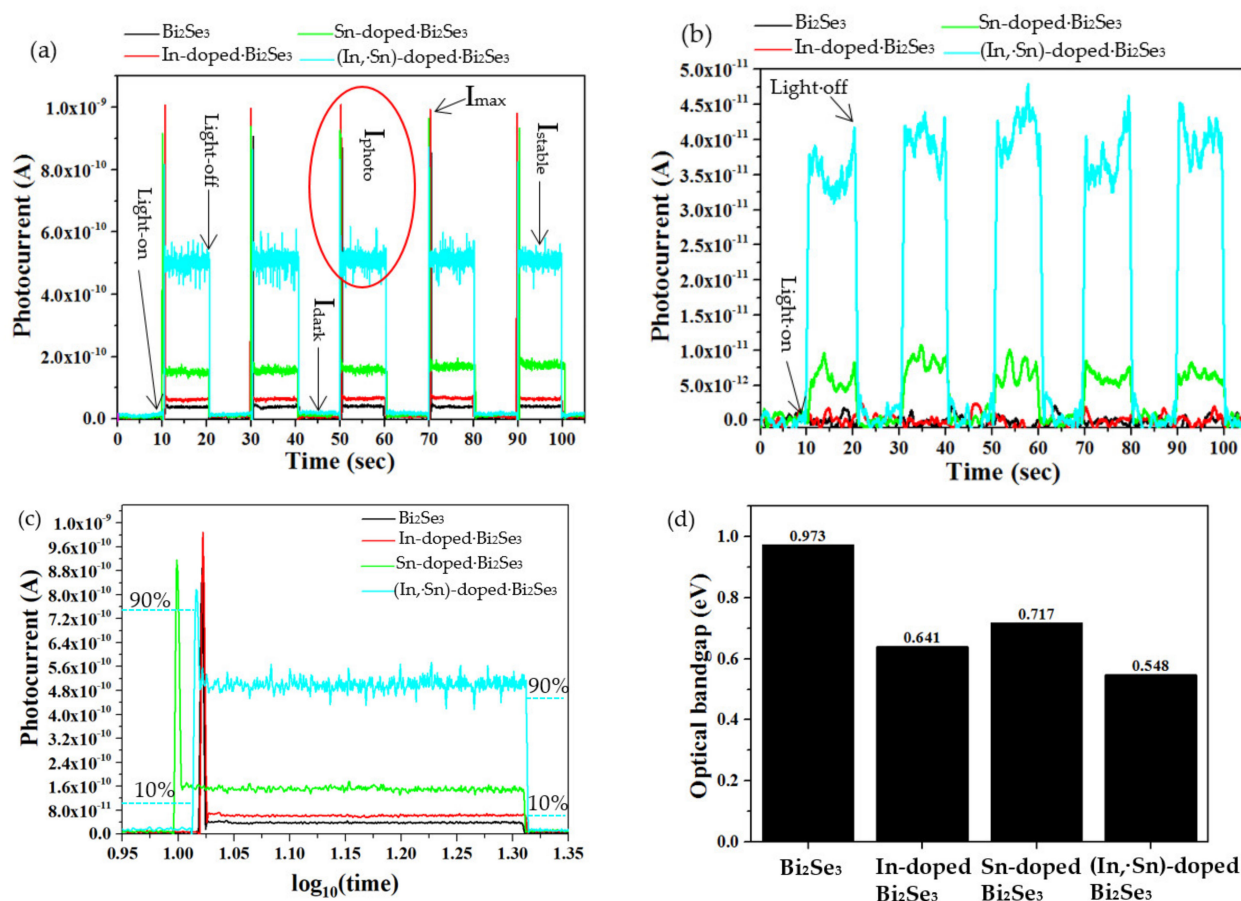


**Figure 6.** Photocurrent plots of pristine, and In-, Sn-, and (In, Sn)-doped  $\text{Bi}_2\text{Se}_3$  nanoplatelets under (a) UV (8 W) and (b) red light (5 W). (c) The variations of the  $\log_{10}(\text{time})$  vs. the photocurrents between the pristine, and In-, Sn-, and (In,Sn)-doped  $\text{Bi}_2\text{Se}_3$  nanoplatelets in the first run of the light-on/light-off cycle. (d) The estimated optical bandgap energies.

**Table 5.** Details of photocurrent measurements of the  $I_{\text{max}}$ ,  $I_{\text{stable}}$ ,  $\Delta I_{\text{decay}}$ ,  $\tau_r$ ,  $t_{\text{decay}}$ ,  $\tau_f$ , and  $I_{\text{photo}}/I_{\text{dark}}$  ratios under the UV light.

Sample	$I_{\text{max}} (\times 10^{-10} \text{ A})$	$I_{\text{stable}} (\times 10^{-10} \text{ A})$	$\Delta I_{\text{decay}} (\times 10^{-10} \text{ A})$	$\tau_r$ (sec)	$t_{\text{decay}}$ (sec)	$\tau_f$ (sec)	$I_{\text{photo}}/I_{\text{dark}}$ (0 V Bias Voltage)
$\text{Bi}_2\text{Se}_3$	8.73	0.40	8.33	0.053	0.091	0.049	7.66
In-doped $\text{Bi}_2\text{Se}_3$	9.98	0.65	9.33	0.051	0.097	0.050	9.29
Sn-doped $\text{Bi}_2\text{Se}_3$	9.36	1.60	7.76	0.044	0.099	0.054	15.8
(In, Sn)-doped $\text{Bi}_2\text{Se}_3$	8.41	5.20	3.21	0.041	0.105	0.066	30.7

Figure 6b presents variations of the photocurrent of the undoped, and In-, Sn-, and (In, Sn)-doped  $\text{Bi}_2\text{Se}_3$  nanoplatelets under red light. Both undoped and In-doped  $\text{Bi}_2\text{Se}_3$  generate no photocurrent, whereas Sn- and (In, Sn)-doped  $\text{Bi}_2\text{Se}_3$  generate a photocurrent of  $0.5 \times 10^{-10}$  and  $3.5 \times 10^{-10}$  A when the red light is turned on. These results reveal that the photosensitivity of  $\text{Bi}_2\text{Se}_3$  nanoplatelets to a red light is greatly improved by the dopants, and especially by the co-dopants In and Sn. The  $I_{\text{photo}}/I_{\text{dark}}$  ratios of the undoped, and In-, Sn-, and (In, Sn)-doped  $\text{Bi}_2\text{Se}_3$  nanoplatelets are, respectively, estimated as 1, 1,

20.9, and 52.2, as shown in Figure S4b. The co-dopants of In and Sn enhance the Bi<sub>2</sub>Se<sub>3</sub> nanoplatelets 52.2 times higher than that of the undoped one.

### 3.5.2. Effects of the Defect Structure and Optical Bandgap on Photocurrent

Figure 6d shows that the optical bandgaps, estimated from the Tauc plot [60], of the undoped, as well as In-, Sn-, and (In, Sn)-doped Bi<sub>2</sub>Se<sub>3</sub> nanoplatelets, are 0.973, 0.641, 0.717, and 0.548 eV, respectively. These bandgaps are estimated by the following equation of  $(\alpha h\nu)^n = A(h\nu - E_g)$ , where  $\alpha$  is the absorption coefficient,  $h$  is the Planck's constant,  $\nu$  is the light frequency,  $n$  is the characteristic coefficient of materials,  $A$  is a constant, and  $E_g$  is the bandgap. For the direct bandgap of the Bi<sub>2</sub>Se<sub>3</sub>,  $n$  is 2. Their absorbance spectra, which were recorded by FPA-FTIR, are shown in Figure S5. Each individual Tauc plot of the pristine, In-, Sn-, and (In,Sn)-doped Bi<sub>2</sub>Se<sub>3</sub> nanoplatelets is demonstrated in Figure S6. These small bandgaps show that the incident UV (~3.4 eV) and red (~1.37–1.77 eV) light easily generate photo-induced electrons and holes. A photocurrent is therefore detectable in all of the samples of interest. However, the variously doped Bi<sub>2</sub>Se<sub>3</sub> nanoplatelets exhibit significantly different photocurrents. Defect structures are the dominant factor that affects the photocurrent. Possible defects are  $(In^{3+}_{Bi^{3+}})$ ,  $(In^{3+}_{V_0})$ ,  $(Sn^{4+}_{Bi^{3+}})$ ,  $(V^0_{Bi^{3+}})$ , and  $(Sn^{2+}_{Bi^{3+}})$ , where  $(In^{3+}_{Bi^{3+}})$  a neutral defect;  $(In^{3+}_{V_0})$  and  $(Sn^{4+}_{Bi^{3+}})$  are donor defects and supply additional electrons; and  $(V^0_{Bi^{3+}})$  and  $(Sn^{2+}_{Bi^{3+}})$  are acceptor defects and supply additional holes.  $(V^0_{Bi^{3+}})$  is the main defect in undoped Bi<sub>2</sub>Se<sub>3</sub>, whose photocurrent under UV or red light is, therefore, the lowest or ~0 A.  $(In^{3+}_{Bi^{3+}})$  and  $(In^{3+}_{V_0})$  instead of  $(V^0_{Bi^{3+}})$  are the main defects in In-doped Bi<sub>2</sub>Se<sub>3</sub>, and therefore, a photocurrent under UV is detected therein. However, no photocurrent is detected under red light, owing to the lower electron concentration and faster recombination of electrons and holes.  $(Sn^{4+}_{Bi^{3+}})$  rather than  $(Sn^{2+}_{Bi^{3+}})$  and  $(V^0_{Bi^{3+}})$  is the main defect in Sn-doped Bi<sub>2</sub>Se<sub>3</sub> nanoplatelets; hence, more electrons than undoped and In-doped Bi<sub>2</sub>Se<sub>3</sub> nanoplatelets can be supplied and generate a high photocurrent under UV or red light. Accordingly, Sn-doped Bi<sub>2</sub>Se<sub>3</sub> nanoplatelets exhibit a higher photocurrent than undoped and In-doped Bi<sub>2</sub>Se<sub>3</sub> nanoplatelets.  $(V^0_{Bi^{3+}})$  and  $(Sn^{2+}_{Bi^{3+}})$  are not the main defects. Rather,  $(In^{3+}_{V_0})$ ,  $(Sn^{4+}_{Bi^{3+}})$ , and  $(In^{3+}_{Bi^{3+}})$  are the main defects in (In, Sn)-doped Bi<sub>2</sub>Se<sub>3</sub> nanoplatelets.  $(In^{3+}_{V_0})$  and  $(Sn^{4+}_{Bi^{3+}})$  can supply more additional electrons than undoped, as well as In- and Sn-doped Bi<sub>2</sub>Se<sub>3</sub> nanoplatelets, to generate the highest photocurrent. Therefore, the (In, Sn)-doped Bi<sub>2</sub>Se<sub>3</sub> nanoplatelets have the highest photocurrents under UV and red light than do undoped, as well as In-, and Sn-doped Bi<sub>2</sub>Se<sub>3</sub> nanoplatelets. Based on the above discussion, the reduced optical bandgap of the doped Bi<sub>2</sub>Se<sub>3</sub> nanoplatelets is a minor factor that affects the photocurrent. The type of defect that is generated by doping has a greater effect on the photodetection sensitivity than the corresponding reduction of the optical bandgap.

## 4. Conclusions

(In, Sn)-doped Bi<sub>2</sub>Se<sub>3</sub> nanoplatelets under UV (8 W) and red light (5 W) have a higher  $I_{\text{photo}}/I_{\text{dark}}$  ratio of 30.7 and 52.2 and a stable photocurrent of  $5.20 \times 10^{-10}$  and  $0.35 \times 10^{-10}$  A, respectively, higher than that of the undoped Bi<sub>2</sub>Se<sub>3</sub> nanoplatelets (UV light: 7.66,  $0.4 \times 10^{-10}$  A; red light: 1,  $2.38 \times 10^{-13}$  A). (In, Sn)-doped Bi<sub>2</sub>Se<sub>3</sub> nanoplatelets have a shorter photocurrent rise time (0.041 s) and a longer decay time (0.105 s) than undoped Bi<sub>2</sub>Se<sub>3</sub> nanoplatelets (0.053 and 0.091 s) by about 22.6% and 15.3%, respectively. These results suggest that photodetection under UV and red light by pristine Bi<sub>2</sub>Se<sub>3</sub> nanoplatelets can be improved by doping with In and Sn. The optical bandgap of pristine Bi<sub>2</sub>Se<sub>3</sub> nanoplatelets is 0.973 eV; it can be reduced to 0.641, 0.717, and 0.548 eV, corresponding to reductions of 34.1%, 26.3%, and 43.7% by doping with In, Sn, and both In and Sn. Based on XRD, XPS, FESEM-EDS, and Raman spectra,  $(In^{3+}_{V_0})$ ,  $(Sn^{4+}_{Bi^{3+}})$ ,  $(In^{3+}_{Bi^{3+}})$ ,  $(V^0_{Bi^{3+}})$ , and  $(Sn^{2+}_{Bi^{3+}})$  were formed during the synthesis of nanoplatelets, and structural defects  $(In^{3+}_{V_0})$  and  $(Sn^{4+}_{Bi^{3+}})$  significantly improved the photocurrent of (In, Sn)-doped Bi<sub>2</sub>Se<sub>3</sub> nanoplatelets under UV and red light. This work also reveals that In or Sn dopant has no effect on the crystal structure of rhombohedral Bi<sub>2</sub>Se<sub>3</sub>. These results suggest that

the photodetection sensitivity of Bi<sub>2</sub>Se<sub>3</sub> nanoplatelets is dominated by the defect structures that are generated by doping, as well as by the consequent reduction of optical bandgap energy. The co-dopants In and Sn further enhance the ability of Bi<sub>2</sub>Se<sub>3</sub> nanoplatelets to respond to UV and red light.

**Supplementary Materials:** The following are available online at <https://www.mdpi.com/article/10.3390/nano11051352/s1>, Figure S1: Schematic of the furnace, crucible, substrate, and operating conditions, Figure S2: Schematic diagram of the photocurrent measurement system, Figure S3: FESEM cross-sectional images of (a) pristine, (b) In-, (c) Sn-, and (d) (In,Sn)-doped Bi<sub>2</sub>Se<sub>3</sub> nanoplatelets, Figure S4: Comparisons of the current in logarithmic scale vs. time under the (a) UV and (b) red light, Figure S5: FPA–FTIR absorbance and (b) estimated optical bandgaps of the pristine, and In-, Sn-, and (In,Sn)-doped Bi<sub>2</sub>Se<sub>3</sub> nanoplatelets, Figure S6: The estimated optical bandgaps of (a) pristine, and (b) In-, (c) Sn-, and (d) (In,Sn)-doped Bi<sub>2</sub>Se<sub>3</sub> nanoplatelets, Table S1: Lists of the Bi<sub>2</sub>Se<sub>3</sub>-based photodetectors, Table S2: Lists of the Bi<sub>2</sub>Se<sub>3</sub> doped with various elements and the variation of the bandgap energy.

**Author Contributions:** Conceptualization, F.-S.S. and H.C.S.; methodology, F.-S.S., H.C.S., and C.-C.W.; software, C.-C.W.; validation, C.-C.W.; formal analysis, C.-C.W.; investigation, C.-C.W.; resources, H.C.S. and F.-S.S.; data curation, C.-C.W.; writing—original draft preparation, C.-C.W.; writing—review and editing, H.C.S. and F.-S.S.; visualization, C.-C.W.; supervision, H.C.S. and F.-S.S.; project administration, H.C.S.; funding acquisition, H.C.S. All authors have read and agreed to the published version of the manuscript.

**Funding:** This research was funded by the Ministry of Science and Technology (MOST) of Taiwan, the Republic of China, Grant Number MOST 108-2221-E-034-010.

**Institutional Review Board Statement:** Not applicable.

**Informed Consent Statement:** Not applicable.

**Data Availability Statement:** Data are contained within the article.

**Acknowledgments:** The authors gratefully acknowledge the financial support of the Ministry of Science and Technology (MOST) of Taiwan, the Republic of China, under contract MOST 108-2221-E-034-010.

**Conflicts of Interest:** The authors declare no conflict of interest.

## References

1. Lawal, A.; Shaari, A.; Ahmed, R.; Jarkoni, N. First-principles many-body comparative study of Bi<sub>2</sub>Se<sub>3</sub> crystal: A promising candidate for broadband photodetector. *Phys. Lett. A* **2017**, *381*, 2993–2999. [[CrossRef](#)]
2. Ren, Z.; Taskin, A.A.; Sasaki, S.; Segawa, K.; Ando, Y. Large bulk resistivity and surface quantum oscillations in the topological insulator. *Phys. Rev. B* **2010**, *82*, 241306. [[CrossRef](#)]
3. Zhang, H.; Liu, C.X.; Qi, X.L.; Dai, X.; Fang, Z.; Zhang, S.C. Topological insulators in Bi<sub>2</sub>Se<sub>3</sub>, Bi<sub>2</sub>Te<sub>3</sub> and Sb<sub>2</sub>Te<sub>3</sub> with a single Dirac cone on the surface. *Nat. Phys.* **2009**, *5*, 438–442. [[CrossRef](#)]
4. Zhang, M.; Liu, L.G.; Wang, D.; An, X.Y.; Yang, H. Enhancement of surface state contribution in cadmium doped Bi<sub>2</sub>Se<sub>3</sub> single crystal. *J. Alloys Compd.* **2019**, *806*, 180–186. [[CrossRef](#)]
5. Salvato, M.; Scagliotti, M.; De Crescenzi, M.; Castrucci, P.; De Matteis, F.; Crivellari, M.; Cresi, S.P.; Catone, D.; Bauch, T.; Lombardi, F. Stoichiometric Bi<sub>2</sub>Se<sub>3</sub> topological insulator ultra-thin films obtained through a new fabrication process for optoelectronic applications. *Nanoscale* **2020**, *12*, 12405. [[CrossRef](#)]
6. Irfan, B.; Sahoo, S.; Gaur, A.P.S.; Ahmadi, M.; Guinel, M.J.F.; Katiyar, R.S.; Chatterjee, R. Temperature dependent Raman scattering studies of three dimensional topological insulators Bi<sub>2</sub>Se<sub>3</sub>. *J. Appl. Phys.* **2014**, *115*, 173506. [[CrossRef](#)]
7. Schönherr, P.; Collins-McIntyre, L.J.; Zhang, S.; Kusch, P.; Reich, S.; Giles, T.; Daisenberger, D.; Prabhakaran, D.; Hesjedal, T. Vapour-liquid-solid growth of ternary Bi<sub>2</sub>Se<sub>2</sub>Te nanowires. *Nanoscale Res. Lett.* **2014**, *9*, 127. [[CrossRef](#)] [[PubMed](#)]
8. Meyer, N.; Geishendorf, K.; Walowski, J.; Thomas, A.; Munzenberg, M. Photocurrent measurements in topological insulator Bi<sub>2</sub>Se<sub>3</sub> nanowires. *Appl. Phys. Lett.* **2020**, *116*, 172402. [[CrossRef](#)]
9. Yue, C.; Jiang, S.; Zhu, H.; Chen, L.; Sun, Q.; Zhang, D.W. Device applications of synthetic topological insulator nanostructures. *Electronics* **2018**, *7*, 225. [[CrossRef](#)]
10. Tian, W.; Yu, W.; Shi, J.; Wang, Y. The property, preparation and application of topological insulators: A Review. *Materials* **2017**, *10*, 814. [[CrossRef](#)]

11. Mishra, S.K.; Satpathy, S.; Jepsen, O. Electronic structure and thermoelectric properties of bismuth telluride and bismuth selenide. *J. Phys. Condens. Matter*. **1997**, *9*, 461–470. [[CrossRef](#)]
12. Hsieh, D.; Xia, Y.; Wray, L.; Qian, D.; Pal, A.; Dil, J.H.; Meier, F.; Osterwalder, J.; Bihlmayer, G.; Kane, C.L.; et al. First direct observation of spin-textures in topological insulators: Spin-resolved ARPES as a probe of topological quantum spin Hall effect and Berry's phase. *Science* **2009**, *323*, 919–933. [[CrossRef](#)]
13. Fei, F.; Zhang, S.; Zhang, M.; Shah, S.A.; Song, F.; Wang, X.; Wang, B. The material efforts for quantized Hall devices based on topological insulators. *Adv. Mater.* **2020**, *32*, 1904593. [[CrossRef](#)] [[PubMed](#)]
14. Yao, J.; Shao, J.; Wang, Y.; Zhao, Z.; Yang, G. Ultra-broadband and high response of the Bi<sub>2</sub>Te<sub>3</sub>-Si heterojunction and its application as a photodetector at room temperature in harsh working environments. *Nanoscale* **2015**, *7*, 12535–12541. [[CrossRef](#)]
15. Jung, M.; Lee, J.; Koo, J.; Park, J.; Song, Y.W.; Lee, K.; Lee, S.; Lee, J.H. A femtosecond pulse fiber laser at 1935 nm using a bulk-structured Bi<sub>2</sub>Te<sub>3</sub> topological insulator. *Opt. Express* **2014**, *22*, 7865–7874. [[CrossRef](#)]
16. Liu, B.; Xie, W.; Li, H.; Wang, Y.; Cai, D.; Wang, D.; Wang, L.; Liu, Y.; Li, Q.; Wang, T. Surrounding sensitive electronic properties of Bi<sub>2</sub>Te<sub>3</sub> nanoplates-potential sensing applications of topological insulators. *Sci. Rep.* **2014**, *4*, 4639. [[CrossRef](#)] [[PubMed](#)]
17. Götte, M.; Joppe, M.; Dahm, T. Pure spin current devices based on ferromagnetic topological insulators. *Sci. Rep.* **2016**, *6*, 36070. [[CrossRef](#)] [[PubMed](#)]
18. Fan, Y.; Upadhyaya, P.; Kou, X.; Lang, M.; Takei, S.; Wang, Z.; Tang, J.; He, L.; Chang, L.T.; Montazeri, M.; et al. Magnetization switching through giant spin-orbit torque in a magnetically doped topological insulator heterostructure. *Nat. Mater.* **2014**, *13*, 699–704. [[CrossRef](#)]
19. Stern, A.; Lindner, N.H. Topological quantum computation-from basic concepts to first experiments. *Science* **2013**, *339*, 179–1184. [[CrossRef](#)] [[PubMed](#)]
20. Qi, X.L.; Zhang, S.C. Topological insulators and superconductors. *Rev. Mod. Phys.* **2011**, *83*, 1057–1110.
21. Lee, C.W.; Kim, G.H.; Kang, S.G.; Kang, M.A.; An, K.S.; Kim, H.; Lee, Y.K. Growth behavior of Bi<sub>2</sub>Te<sub>3</sub> and Sb<sub>2</sub>Te<sub>3</sub> thin films on graphene substrate grown by plasma-enhanced chemical vapor deposition. *Phys. Status Solidi RRL* **2017**, *11*, 1600369. [[CrossRef](#)]
22. Hwang, T.H.; Kim, H.S.; Kim, H.; Kim, J.S.; Doh, Y.J. Electrical detection of spin-polarized current in topological insulator Bi<sub>1.5</sub>Sb<sub>0.5</sub>Te<sub>1.7</sub>Se<sub>1.3</sub>. *Curr. Appl. Phys.* **2019**, *19*, 917–923. [[CrossRef](#)]
23. Fei, F.; Wei, Z.; Wang, Q.; Lu, P.; Wang, S.; Qin, Y.; Pan, D.; Zhao, B.; Wang, X.; Sun, J.; et al. Solvothermal synthesis of lateral heterojunction Sb<sub>2</sub>Te<sub>3</sub>/Bi<sub>2</sub>Te<sub>3</sub> nanoplates. *Nano Lett.* **2015**, *15*, 5905–5911. [[CrossRef](#)] [[PubMed](#)]
24. Bansal, N.; Cho, M.R.; Brahlek, M.; Koirala, N.; Horibe, Y.; Jing, C.; Wu, W.; Yun, D.P.; Oh, S. Transferring MBE-grown topological insulator films to arbitrary substrates and metal-insulator transition via Dirac gap. *Nano Lett.* **2014**, *14*, 1343–1348. [[CrossRef](#)]
25. Zastrow, S.; Gooth, J.; Boehnert, T.; Heiderich, S.; Toellner, W.; Heimann, S.; Schulz, S.; Nielsch, K. Thermoelectric transport and Hall measurements of low defect Sb<sub>2</sub>Te<sub>3</sub> thin films grown by atomic layer deposition. *Semicond. Sci. Technol.* **2013**, *28*, 035010. [[CrossRef](#)]
26. Bendt, G.; Zastrow, S.; Nielsch, K.; Mandal, P.S.; Sánchezbarriga, J.; Rader, O.; Schulz, S. Deposition of topological insulator Sb<sub>2</sub>Te<sub>3</sub> films by an MOCVD process. *J. Mater. Chem. A* **2014**, *2*, 8215–8222. [[CrossRef](#)]
27. Le, P.H.; Wu, K.H.; Luo, C.W.; Leu, J. Growth and characterization of topological insulator Bi<sub>2</sub>Se<sub>3</sub> thin films on SrTiO<sub>3</sub> using pulsed laser deposition. *Thin Solid Films* **2013**, *534*, 659–665. [[CrossRef](#)]
28. Fang, B.; Zeng, Z.; Yan, X.; Hu, Z. Effects of annealing on thermoelectric properties of Sb<sub>2</sub>Te<sub>3</sub> thin films prepared by radio frequency magnetron sputtering. *J. Mater. Sci. Mater. Electron.* **2013**, *24*, 1105–1111. [[CrossRef](#)]
29. Nam, H.; Xu, Y.; Miotkowski, I.; Tian, J.; Chen, Y.P.; Liu, C.; Hasan, M.Z.; Zhu, W.; Fiete, G.A.; Shih, C.K. Microscopic investigation of Bi<sub>2-x</sub>Sb<sub>x</sub>Te<sub>3-x</sub>Se<sub>y</sub> systems: On the origin of a robust intrinsic topological insulator. *J. Phys. Chem. Solids* **2019**, *128*, 251–257. [[CrossRef](#)]
30. Bhattacharyya, B.; Sharma, A.; Kaur, M.; Singh, B.P.; Husale, S. Highly responsive broadband photodetection in topological insulator-Carbon nanotubes based heterostructure. *J. Alloys Compd.* **2021**, *851*, 156759. [[CrossRef](#)]
31. Zhang, H.; Song, Z.; Li, D.; Xu, Y.; Li, J.; Bai, C.; Man, B. Near-infrared photodetection based on topological insulator P-N heterojunction of SnTe/Bi<sub>2</sub>Se<sub>3</sub>. *Appl. Surf. Sci.* **2020**, *509*, 145290. [[CrossRef](#)]
32. Li, X.M.; Zhao, K.; Ni, H.; Zhao, S.Q.; Xiang, W.F.; Lu, Z.Q.; Yue, Z.J.; Wang, F.; Kong, Y.C.; Wong, H.K. Voltage tunable photodetecting properties of La<sub>0.4</sub>Ca<sub>0.6</sub>MnO<sub>3</sub> films grown on miscut LaSrAlO<sub>4</sub> substrates. *Appl. Phys. Lett.* **2010**, *97*, 044104. [[CrossRef](#)]
33. Huang, S.M.; Huang, S.J.; Yan, Y.J.; Yu, S.H.; Chou, M.; Yang, H.W.; Chang, Y.S.; Chen, R.S. Extremely high-performance visible light photodetector in the Sb<sub>2</sub>SeTe<sub>2</sub> nanoflake. *Sci. Rep.* **2017**, *7*, 45413. [[CrossRef](#)] [[PubMed](#)]
34. Sharma, A.; Bhattacharyya, B.; Srivastava, A.K.; Senguttuvan, T.D.; Husale, S. High performance broadband photodetector using fabricated nanowires of bismuth selenide. *Sci. Rep.* **2016**, *6*, 19138. [[CrossRef](#)] [[PubMed](#)]
35. Yang, M.; Han, Q.; Liu, X.; Han, J.; Zhao, Y.; He, L.; Gou, J.; Wu, Z.; Wang, X.; Wang, J. Ultrahigh stability 3D TI Bi<sub>2</sub>Se<sub>3</sub>/MoO<sub>3</sub> thin film heterojunction infrared photodetector at optical communication waveband. *Adv. Funct. Mater.* **2020**, *30*, 1909659. [[CrossRef](#)]
36. Pejova, B.; Grozdanov, I. Chemical deposition and characterization of glassy bismuth(III) selenide thin films. *Thin Solid Films* **2002**, *408*, 6–10. [[CrossRef](#)]
37. Pramanik, P.; Bhattacharya, R.N.A. Mondal, A chemical method for the deposition of thin films of Bi<sub>2</sub>Se<sub>3</sub>. *J. Electrochem. Soc.* **1980**, *127*, 1857. [[CrossRef](#)]

38. Garcia, V.M.; Nair, M.T.S.; Nair, P.K.; Zingaro, R.A. Chemical deposition of bismuth selenide thin films using N,N-dimethylselenourea. *Semicond. Sci. Technol.* **1997**, *12*, 645–653.
39. Manjulavalli, T.E.; Balasubramanian, T.; Nataraj, D. Structural and optical properties of thermally evaporated Bi<sub>2</sub>Se<sub>3</sub> thin film. *Chalcogenide Lett.* **2008**, *5*, 297–302.
40. Augustine, S.; Ampili, S.; Kang, J.K.; Mathai, E. Structural, electrical and optical properties of Bi<sub>2</sub>Se<sub>3</sub> and Bi<sub>2</sub>Se<sub>(3-x)</sub>Te<sub>x</sub> thin films. *Mater. Res. Bull.* **2005**, *40*, 1314–1325. [[CrossRef](#)]
41. Alemi, A.; Babalou, A.; Dolatyari, M.; Klein, A.; Meyer, G. Hydrothermal synthesis of Nd<sup>III</sup> doped Bi<sub>2</sub>Se<sub>3</sub> nanoflowers and their physical properties. *Z. Anorg. Allg. Chem.* **2009**, *635*, 2053–2057. [[CrossRef](#)]
42. Zheng, F.; Zhang, Q.; Meng, Q.; Wang, B.; Fan, L.; Zhu, L.; Song, F.; Wang, G. Electronic structures and magnetic properties of rare-earth (Sm, Gd) doped Bi<sub>2</sub>Se<sub>3</sub>. *Chalcogenide Lett.* **2017**, *14*, 551–560.
43. Xin, X.; Guo, C.; Pang, R.; Zhang, M.; Shi, X.; Yang, X.; Zhao, Y. Theoretical and experimental studies of spin polarized carbon doped Bi<sub>2</sub>Se<sub>3</sub>. *Appl. Phys. Lett.* **2019**, *115*, 042401. [[CrossRef](#)]
44. Kobayashi, K.; Ueno, T.; Fujiwara, H.; Yokoya, T.; Akimitsu, J. Unusual upper critical field behavior in Nb-doped bismuth selenides. *Phys. Rev. B* **2017**, *95*, 180503. [[CrossRef](#)]
45. Zhang, G.; Qin, H.; Teng, J.; Guo, J.; Guo, Q.; Dai, X.; Fang, Z.; Wu, K. Quintuple-layer epitaxy of thin films of topological insulator Bi<sub>2</sub>Se<sub>3</sub>. *Appl. Phys. Lett.* **2009**, *95*, 053114. [[CrossRef](#)]
46. Wagner, C.D.; Riggs, W.M.; Davis, L.E.; Moulder, J.F.; Muilenberg, G.E. *Hand Book of X-ray Photoelectron Spectroscopy*; Perkin-Elmer Corporation: Eden Prairie, MN, USA, 1979; p. 162.
47. Meng, A.; Yuan, X.; Shen, T.; Li, Z.; Jiang, Q.; Xue, H.; Lin, Y.; Zhao, J. One-step synthesis of flower-like Bi<sub>2</sub>O<sub>3</sub>/Bi<sub>2</sub>Se<sub>3</sub> nanoarchitectures and NiCoSe<sub>2</sub>/Ni<sub>0.85</sub>Se nanoparticles with appealing rate capability for the construction of high-energy and long-cycle-life asymmetric aqueous batteries. *J. Mater. Chem. A* **2019**, *7*, 17613. [[CrossRef](#)]
48. Green, A.J.; Dey, S.; An, Y.Q.; O'Brien, B.; O'Mullane, S.; Thiel, B.; Diebold, A.C. Surface oxidation of the topological insulator Bi<sub>2</sub>Se<sub>3</sub>. *J. Vac. Sci. Technol. A* **2016**, *34*, 061403. [[CrossRef](#)]
49. Hobbs, R.G.; Schmidt, M.; Bolger, C.T.; Georgiev, Y.M.; Fleming, P.; Morris, M.A.; Petkov, N.; Holmes, J.D.; Xiu, F.; Wang, K.L.; et al. Resist–substrate interface tailoring for generating high-density arrays of Ge and Bi<sub>2</sub>Se<sub>3</sub> nanowires by electron beam lithography. *J. Vac. Sci. Technol. B* **2012**, *30*, 041602. [[CrossRef](#)]
50. Botcha, V.D.; Hong, Y.; Huang, Z.; Li, Z.; Liu, Q.; Wu, J.; Lu, Y.; Liu, X. Growth and thermal properties of various In<sub>2</sub>Se<sub>3</sub> nanostructures prepared by single step PVD technique. *J. Alloys Compd.* **2019**, *773*, 698–705. [[CrossRef](#)]
51. Zhang, X.; Liu, Y.; Zhang, G.; Wang, Y.; Zhang, H.; Huang, F. Thermal decomposition of bismuth oxysulfide from photoelectric Bi<sub>2</sub>O<sub>2</sub>S to superconducting Bi<sub>4</sub>O<sub>4</sub>S<sub>3</sub>. *ACS Appl. Mater. Interfaces* **2015**, *7*, 4442–4448. [[CrossRef](#)]
52. Lu, D.; Yue, C.; Luo, S.; Li, Z.; Xue, W.; Qi, X.; Zhong, J. Phase controllable synthesis of SnSe and SnSe<sub>2</sub> films with tunable photoresponse properties. *Appl. Surf. Sci.* **2021**, *541*, 148615. [[CrossRef](#)]
53. Mukhokosi, E.P.; Krupanidhi, S.B.; Nanda, K.K. Band gap engineering of hexagonal SnSe<sub>2</sub> nanostructured thin films for infra-red photodetection. *Sci. Rep.* **2017**, *7*, 15215. [[CrossRef](#)] [[PubMed](#)]
54. Zhang, H.; Zhang, X.; Liu, C.; Lee, S.T.; Jie, J. High-responsivity, high-detectivity, ultrafast topological insulator Bi<sub>2</sub>Se<sub>3</sub>/silicon heterostructure broadband photodetectors. *ACS Nano* **2016**, *10*, 5113–5122. [[CrossRef](#)]
55. Kimura, K.; Hayashi, K.; Yashina, L.V.; Happo, N.; Nishioka, T.; Yamamoto, Y.; Ebisu, Y.; Ozaki, T.; Hosokawa, S.; Matsushita, T.; et al. Local structural analysis of In-doped Bi<sub>2</sub>Se<sub>3</sub> topological insulator using X-ray fluorescence holography. *Surf. Interface Anal.* **2019**, *51*, 51–55. [[CrossRef](#)]
56. Yuan, J.; Zhao, M.; Yu, W.; Lu, Y.; Chen, C.; Xu, M.; Li, S.; Loh, K.P.; Bao, Q. Raman spectroscopy of two-dimensional Bi<sub>2</sub>Te<sub>x</sub>Se<sub>3-x</sub> platelets produced by solvothermal method. *Materials* **2015**, *8*, 5007–5017. [[CrossRef](#)]
57. Pu, X.Y.; Zhao, K.; Liu, Y.; Wei, Z.T.; Jin, R.; Yang, X.S.; Zhao, Y. Structural and transport properties of iridium-doped Bi<sub>2</sub>Se<sub>3</sub> topological insulator crystals. *J. Alloys Compd.* **2017**, *694*, 272–275. [[CrossRef](#)]
58. Shahil, K.M.F.; Hossain, M.Z.; Goyal, V.; Balandin, A.A. Micro-Raman spectroscopy of mechanically exfoliated few-quintuple layers of Bi<sub>2</sub>Te<sub>3</sub>, Bi<sub>2</sub>Se<sub>3</sub>, and Sb<sub>2</sub>Te<sub>3</sub> materials. *J. Appl. Phys.* **2012**, *111*, 054305. [[CrossRef](#)]
59. Basumatary, P.; Agarwal, P. Photocurrent transient measurements in MAPbI<sub>3</sub> thin films. *J. Mater. Sci. Mater. El.* **2020**, *31*, 10047–10054. [[CrossRef](#)]
60. Arumugam, J.; Raj, A.D.; Irudayaraj, A.A.; Thambidurai, M. Solvothermal synthesis of Bi<sub>2</sub>S<sub>3</sub> nanoparticles and nanorods towards solar cell application. *Mater. Lett.* **2018**, *220*, 28–31. [[CrossRef](#)]